

Detection and Longitudinal Tracking of Pigmented Skin Lesions in 3D Total-Body Skin Textured Meshes

Mengliu Zhao*, Jeremy Kawahara*, Sajjad Shamanian, Kumar Abhishek, Priyanka Chandrashekar, and Ghassan Hamarneh

Abstract—We present an automated approach to detect and longitudinally track skin lesions on 3D total-body skin surfaces scans. The acquired 3D mesh of the subject is unwrapped to a 2D texture image, where a trained region convolutional neural network (R-CNN) localizes the lesions within the 2D domain. These detected skin lesions are mapped back to the 3D surface of the subject and, for subjects imaged multiple times, the anatomical correspondences among pairs of meshes and the geodesic distances among lesions are leveraged in our longitudinal lesion tracking algorithm.

We evaluated the proposed approach using three sources of data. Firstly, we augmented the 3D meshes of human subjects from the public FAUST dataset with a variety of poses, textures, and images of lesions. Secondly, using a handheld structured light 3D scanner, we imaged a mannequin with multiple synthetic skin lesions at selected location and with varying shapes, sizes, and colours. Finally, we used 3DBodyTex, a publicly available dataset composed of 3D scans imaging the colored (textured) skin of 200 human subjects. We manually annotated locations that appeared to the human eye to contain a pigmented skin lesion as well as tracked a subset of lesions occurring on the same subject imaged in different poses.

Our results, on test subjects annotated by three human annotators, suggest that the trained R-CNN detects lesions at a similar performance level as the human annotators. Our lesion tracking algorithm achieves an average accuracy of 80% when identifying corresponding pairs of lesions across subjects imaged in different poses. As there currently is no other large-scale publicly available dataset of 3D total-body skin lesions, we publicly release the 10 mannequin meshes and over 25,000 3DBodyTex manual annotations, which we hope will further research on total-body skin lesion analysis.

Index Terms—Total Body 3D Imaging, Dermatology Image Analysis, Skin Lesion Detection and Tracking, Deep Learning

I. INTRODUCTION

Skin diseases are the most common reasons for patients to visit general practitioners in studied populations [Schofield et al., 2011]. In the United States, melanoma-related cancer is estimated to increase by 100 thousand cases and cause more than 7000 deaths in 2021 [American Cancer Society, 2021], while the accessibility and wait time to see a dermatologist has become a concern [Feng et al., 2018, Creadore et al., 2021]. Leveraging the ability of artificial intelligence, especially in assisting the diagnosis of whole-body melanoma-related

skin cancer, may improve the early diagnosis efficiency and improve patients’ outcomes [Shellenberger et al., 2016].

When diagnosing a lesion, considering a large region of the skin and changes to lesions over time may provide additional helpful context not available when only considering a localized lesion at a single point in time. For example, visualizing a wide region of the skin may allow for multiple nevi to be detected, which is an important risk factor for melanoma [Gandini et al., 2005]. When monitoring a lesion over time, a nevi that is changing is an additional melanoma risk factor [Abbasi et al., 2004]. As an estimated 30% of melanomas evolve from existing nevi [Pampena et al., 2017], imaging and tracking a lesion across time may lead to a better understanding of how a lesion may transform and allow for early prediction of melanoma [Sondermann et al., 2019], reduce the number of excisions [Tschandl, 2018], and improve the prognosis of certain melanoma risk groups [Haenssle et al., 2010]. Further, clinical studies suggest a benefit to patient outcome through longitudinal total body skin imaging. Monitoring high risk patients with follow-up visits using total body photography has been found to be associated with a greater rate of detecting lower-risk melanomas and overall survival [Strunck et al., 2020]. Combining digital total-body photography and dermoscopy to monitor patients over time has been found to enable early detection of melanoma with a low excision rate [Salerni et al., 2012].

While total body skin imaging and longitudinal monitoring of skin lesions shows promise to improve melanoma detection, the amount of manual intervention required by human dermatologists to monitor and track changes of multiple lesions over the entire body is significant. As such, computer aided approaches to detect lesions over the entire body and track changes to the lesions over time may reduce the required manual intervention and, in addition, serve as a system to flag high risk lesions for review by human dermatologists.

A. Tracking and Detecting Multiple Lesions

The majority of computer aided approaches to analyze pigmented skin lesions rely on static 2D colour images showing a single lesion, with limited works focusing on total-body photography or tracking lesions across time [Celebi et al., 2019, Pathan et al., 2018]. Rather than focusing on a single lesion, a *wide-area* (e.g., torso) region of the body can be imaged, where multiple lesions are visible. Using wide-area

Medical Image Analysis Lab, School of Computing Science, Simon Fraser University, Burnaby V5A 1S6, Canada

*Joint first authors.

Corresponding author: hamarneh@sfu.ca (Ghassan Hamarneh)

images, Lee et al. [2005] proposed an unsupervised approach to segment and count moles from 2D colour images of the back torso, but did not explore tracking lesions across time or incorporate total body images.

Other computer aided approaches explore changes to a *single lesion* across time. For example, to measure changes within a lesion across time, Navarro et al. [2019] proposed to register two dermoscopy images of the same lesion taken at different times and combined an automatic lesion segmentation approach to evaluate how a skin lesion evolves. Their approach assumes the corresponding lesions are known and the images are acquired using dermoscopy, which provide a more controlled field-of-view and scale than non-dermoscopy images.

Combining both wide-area images and lesions imaged over time, McGregor [1998] registered (non-dermoscopy) photographs of human subjects by automatically detecting and selecting a matching subset of the lesions used to transform the images. Their study restricted the imaging to the torso regions and did not explore total body imaging. Mirzaalian et al. [2016] proposed an approach to track skin lesions by detecting lesions on 2D wide-area skin images of the back of a body and matching lesions across images of the same subject using detected anatomical landmarks. Li et al. [2017] proposed a data augmentation strategy to synthesize large body images by blending skin lesion images onto images of back, legs, and chest using Poisson image editing, and then trained a fully convolutional neural network to perform lesion detection and a CNN to track lesions over time by estimating pixel-wise correspondence between a pair of images of the same body part. More recently, Soenksen et al. [2021] proposed a multi-stage workflow for detecting pigmented skin lesions from 2D wide-field images by first using a blob detection algorithm to extract all regions of interest in an image followed by CNN-based classification of these regions as suspicious or non-suspicious skin lesions or other classes (skin only, skin edge, or other background material).

Expanding the imaging field-of-view, *total-body* photography allows for the entire skin (or nearly the entire skin) to be imaged. Korotkov et al. [2015] developed an image acquisition system for photogrammetry-based total body scanning of the skin to automatically acquire overlapping images of the patient’s skin. As the scanning system is in a carefully controlled environment, lesions can be automatically tracked across scans. Korotkov et al. [2019] further extended their system to improve mole matching among images, but did not explore 3D reconstruction of skin surfaces.

The 2014 work by Bogo et al. [2014b] is similar to ours, where Bogo et al. [2014b] performed whole-body 3D imaging, registered body scans acquired at multiple times, detected candidate lesions using linear discriminant analysis, and tracked lesions based on the registered body locations. We differ in our approach in that we use recently developed deep-learning based approaches to both detect lesions and register meshes, where our lesion detection step does not require choosing a threshold to isolate the skin nor post-processing as done in [Bogo et al., 2014b]. For lesion tracking, Bogo et al. [2014b] used a common UV template to map anatomically

corresponding locations to common texture elements within a texture image, while we perform our tracking on the 3D coordinates and consider geodesic distances between pairs of lesions. Finally, we note we use a larger dataset (200 vs. 22 unique subjects) with manually detected lesions (vs. artificially drawn lesions).

B. Longitudinal Skin Datasets with Multiple Lesions

When compared to the large body of literature using static, single lesion images to analyze skin lesions, there are relatively few skin works for tracking multiple lesions across time. This is likely due to the lack of large standardized annotated datasets of longitudinal images available for computer-aided research, prompting a call by clinicians to gather longitudinal skin lesion images to train both clinicians and computer algorithms [Sondermann et al., 2019].

The publicly available FAUST dataset [Bogo et al., 2014a] provides 300 3D body meshes, but lacks skin texture information. Saint et al. [2018] created the dataset 3DBodyTex, which consists of 400 high resolution, 3D texture scans of 100 male and 100 female subjects captured in two different poses. Some lesions are visible on the skin; however, there are no lesion annotations publicly available. To the best of our knowledge, there currently is no large scale longitudinal dataset imaging a wide region of the skin with multiple annotated lesions publicly available. This lack of annotated skin lesion data makes it challenging to train machine learning models that require large amounts of labeled data and to benchmark competing approaches.

C. Contributions

Methodologically, we propose a novel approach to detect and track skin lesions across 3D total-body textured meshes, where the surface of the meshes are unwrapped to yield a 2D texture image, an R-CNN detects the lesions on the 2D texture images, and the detected lesions in 2D are mapped back to 3D coordinates. The detected lesions are tracked in 3D across pairs of meshes of the same subject using an optimization that relies on deep learning-based anatomical correspondences and the geodesic distances between lesions. Our results demonstrate the generalizability of the proposed pipeline through an evaluation using different acquisition systems. To the best of our knowledge, this is the first study to explore hand-held 3D scanning for whole body skin lesion detection, and the largest evaluation of 3D total-body skin lesion tracking using human textured subjects. Further, we release the whole-body dataset of a mannequin imaged with an Artec Eva scanner with synthetic lesions and corresponding lesion annotations, as well as make publicly available¹ over 25,000 manual lesion annotations for 3DBodyTex.

II. METHODS

To detect lesions on the surface of 3D models and track lesions across time, we propose a pipeline (Fig. 1) comprising

¹Full dataset released upon publication. We provide a subset of the data at <http://i.sfu.ca/wfqrbO>, password: `skin3d2021`

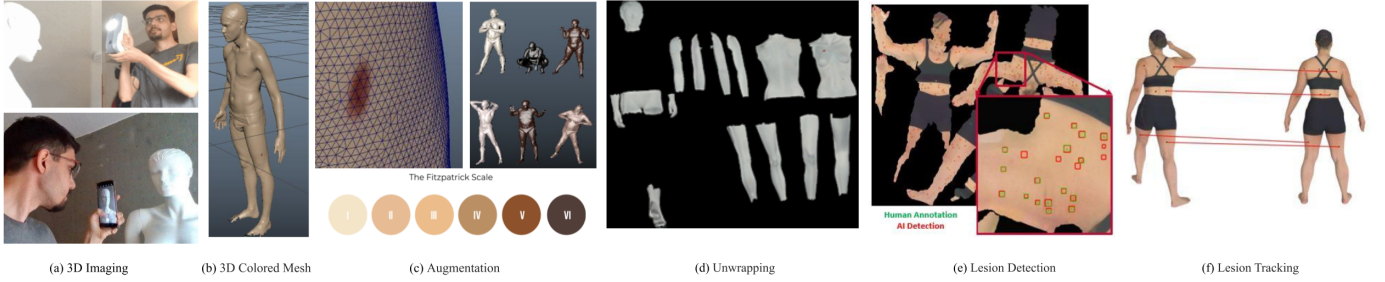


Fig. 1: Proposed pipeline to detect skin lesions on 3D total-body images.

the acquisition of 3D mesh models where skin textures are mapped to 2D texture images, detecting lesions on 2D texture images, and 3D tracking of lesions for longitudinal monitoring. A summary of the mathematical notation used in this paper is provided in Table I.

A scanned 3D object (e.g., mannequin, human subject) is represented as a 3D mesh $\mathcal{M} = (V, F, U, I)$, with N vertices $V \in \mathbb{R}^{N \times 3}$ where a single vertex $v \in V$ describes a 3D spatial coordinate; $f \in F$ is the 3D face set which encodes the edges among the vertices; and $U \in \mathbb{R}^{N \times 2}$ are 2D UV texture coordinates that map vertices V to the texture image $I \in \mathbb{R}^{W \times H \times 3}$, where W and H indicate the width and height of the colour texture image. Given meshes of the same subject scanned at T different points in time $\{\mathcal{M}_t\}_{t=1}^T$, our goal is to detect the skin lesions within each scan, and match the corresponding lesions across the scans.

TABLE I: Summary of Notations

Notation	Description
\mathcal{M}	A 3D mesh
V	A set of 3D vertices
v	A single 3D vertex
U	A set of UV texture coordinates
u	A single UV texture coordinates
I	A 2D texture image
\mathbb{R}	The set of real numbers
ϕ	Region convolutional neural network
θ	The learned parameters of an R-CNN
Y	A set of 2D lesions coordinates
y	2D lesion bounding box coordinates
\hat{Y}	Set of predicted 2D bounding box coordinates
\hat{y}	Predicted 2D lesion bounding box coordinates
\hat{Z}	A set of predicted 3D lesion center coordinates
\hat{z}	Predicted 3D lesion center point coordinates
A	The vertices of the template
R	The set of 3D reconstructed vertices
r	A single 3D reconstructed vertex
π	Matching matrix of 3D vertices
\mathcal{L}	3D matching loss
\mathcal{U}	Unary term of 3D matching loss
\mathcal{B}	Binary term of 3D matching loss
\mathcal{D}	Matching matrix of 3D vertices

A. Detecting Lesions on 2D Texture Images

To detect lesions, we rely on the 2D texture image I . The M lesions $Y \in \mathbb{R}^{M \times 4}$ within I are represented as 2D bounding boxes, where a single lesion $y \in Y$ is composed of four coordinates (left, right, top, and bottom) that define the border of the bounding box. We represent a lesion with

a 2D bounding box since our goal in this work is to detect (i.e., localize and classify the existence of) the lesion from the background skin, which can be obtained via a bounding box, rather than acquiring a precise lesion segmentation. Precisely annotating the boundaries of the lesion is challenging due to the resolution of the texture images. Further, manually annotating 2D bounding boxes is far less time consuming for human annotators compared to 3D delineations.

Using the 2D texture image I and corresponding lesion 2D bounding box annotations Y , we trained a region convolutional neural network (R-CNN) (details in Section IV) to predict 2D bounding box coordinates,

$$\hat{Y} = \phi(I; \theta) \quad (1)$$

where $\phi(\cdot)$ is the R-CNN trained to detect skin lesions with learned parameters θ ; and \hat{Y} are the predicted 2D lesion bounding box coordinates within I . We use these 2D predicted bounding box lesion coordinates to measure the lesion detection performance between human and machine annotations (see results in Section IV-B1). However, for visualization purposes, and for tracking lesions across time, we require the 2D lesion locations to be mapped back to 3D coordinates.

B. Mapping the Detected 2D Lesions onto a 3D Mesh

To visualize the 2D bounding boxes on the 3D mesh, we modify the texture elements based on the coordinates of the lesion bounding boxes \hat{Y} in order to embed the bounding boxes within the original texture image I . The resulting lesion embedded texture image $I_{\hat{Y}}$ (Fig. 2) replaces the original texture image I to show the embedded lesion annotations and texture information on the 3D mesh $\mathcal{M}_{\hat{Y}} = (V, F, U, I_{\hat{Y}})$.

While bounding boxes are well suited for visualizing the localized lesions, for 3D analysis, we represent a lesion with the 3D vertex closest to the UV coordinates of the lesion's 2D center point. Specifically, given the i -th lesion $\hat{y}^{(i)}$ detected within I , we find the index of the UV coordinates closest to the center point of the 2D bounding box,

$$j^* = \operatorname{argmin}_{j \in \{1, \dots, N\}} L_1(u^{(j)}, f(\hat{y}^{(i)})) \quad (2)$$

where $f(\cdot)$ computes the 2D center of the lesion bounding box and converts these image coordinates to the UV domain; $u^{(j)} \in U$ returns the j -th UV coordinates; and $L_1(\cdot)$ computes the L_1 distance between the mesh's UV coordinates and the predicted lesion's UV coordinates. As the indexes of the UV



Fig. 2: A texture image with lesions detected manually (green box) and automatically (red box). The yellow borders indicate overlapping manual and automatic boxes.

coordinates U correspond to the indexes of the vertices V (i.e., the UV coordinates that correspond to $v^{(j)}$ are $u^{(j)}$), we obtain the mesh’s 3D vertex that corresponds to the 2D lesion coordinates by indexing the j^* -th vertex, $v^{(j^*)}$. Thus we map the i -th 2D lesion to the j^* -th 3D vertex within the mesh,

$$\hat{y}^{(i)} \longrightarrow v^{(j^*)} \quad (3)$$

where Eq. 2 is used to determine this mapping.

C. Anatomically Corresponding Vertices Across Scans

The same patient can be scanned at T different times to form a set of 3D meshes $\{\mathcal{M}_t\}_{t=1}^T$. Our goal is to track the lesions across each scan, which requires us to consider the anatomical location of the lesion. However, as the poses of the subject differ across scans, the 3D spatial coordinates alone are unsuitable to directly determine anatomical correspondences across scans. To address this, we use 3D-CODED, a shape deformation network that uses deep learning to match deformable shapes [Groueix et al., 2018, Deprelle et al., 2019]. We use the human template, trained network, and default optimization parameters as provided by 3D-CODED to determine anatomical correspondences of the vertices across scans of the same subject. The full details of the 3D-CODED approach are provided in Groueix et al. [2018], but here we highlight that 3D-CODED outputs reconstructed vertices $R \in \mathbb{R}^{N_A \times 3}$ that map to vertices in a common template $A \in \mathbb{R}^{N_A \times 3}$ (where N_A are the number of vertices within the template) which we use to determine anatomical correspondences. Specifically, given R_t as the reconstructed vertices of \mathcal{M}_t , for the i -th vertex



Fig. 3: The front and back of a subject with manual and automatically annotated lesions after mapping the texture image in Fig. 2 onto a 3D body mesh, where the lines on the body indicate the texture seams.

$v_t^{(i)}$ in \mathcal{M}_t , we find the index j^* of the closest reconstructed vertex,

$$j^* = \underset{j \in \{1, \dots, N_A\}}{\operatorname{argmin}} L_2(r_t^{(j)}, v_t^{(i)}) \quad (4)$$

where $r_t^{(j)} \in R_t$ is the j -th reconstructed vertex; and $L_2(\cdot)$ computes the L_2 distance between the reconstructed and the original vertex. As the reconstructed vertices R_t and R_{t+1} share the common template A , the j^* -th vertex index gives us the anatomically corresponding vertex in R_{t+1} (i.e., $r_t^{(j^*)} \in R_t$ and $r_{t+1}^{(j^*)} \in R_{t+1}$ can have different spatial coordinates, but point to the same anatomical location). Thus we find the anatomically corresponding point in \mathcal{M}_{t+1} by,

$$k^* = \underset{k \in \{1, \dots, N_{t+1}\}}{\operatorname{argmin}} L_2(v_{t+1}^{(k)}, r_{t+1}^{(j^*)}) \quad (5)$$

where N_{t+1} is the number of vertices in \mathcal{M}_{t+1} ; the vertex $v_{t+1}^{(k)} \in \mathcal{M}_{t+1}$; and $r_{t+1}^{(j^*)} \in R_{t+1}$ is the vertex reconstructed from \mathcal{M}_{t+1} with the j^* -th index as determined by Eq. 4. With the k^* -th index, we then determine that $v_{t+1}^{(k^*)} \in \mathcal{M}_{t+1}$ corresponds anatomically to $v_t^{(i)} \in \mathcal{M}_t$, which allows us to map anatomically corresponding vertices in \mathcal{M}_k to vertices in \mathcal{M}_{k+1} .

D. Tracking Lesions Across Poses and Time

Given a pair of meshes, \mathcal{M}_t and \mathcal{M}_{t+1} , of the same subject imaged at different times and corresponding lesions, \hat{Y}_t and \hat{Y}_{t+1} , detected on the 2D texture images (Eq. 1), we map the center points of the 2D detected lesions to the closest vertices on the corresponding 3D meshes (Eq. 3). We denote these 3D vertices that correspond to lesion center points as $\hat{Z}_t \in V_t$, where \hat{Z}_t is a subset of the vertices found within the original

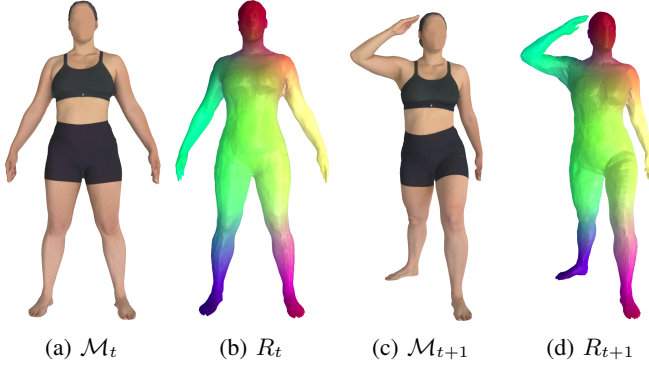


Fig. 4: Correspondence between two 3D meshes. (a) and (c) show meshes of the same subject in different poses. (b) and (d) show the reconstructed meshes, where the colours indicate vertex correspondence.

mesh's vertices V_t (i.e., $\hat{z}_t^{(i)} \in \hat{Z}_t$ is the 3D coordinates of the i -th lesion $\hat{y}_t^{(i)}$ detected on the 2D texture image).

We seek to establish correspondence between the lesions $\hat{z}_t \in \hat{Z}_t$ and $\hat{z}_{t+1} \in \hat{Z}_{t+1}$ of any two (temporally adjacent) meshes \mathcal{M}_t and \mathcal{M}_{t+1} . The correspondence would allow for tracking changes (e.g., size and appearance) in a particular lesion across time (similar to previous work on 2D skin images [Mirzaalian et al., 2016]). To this end, we optimize the matching function,

$$\pi : (\hat{z}_t, \hat{z}_{t+1}) \longrightarrow \{0, 1\}, \quad (6)$$

which gives 1, when its input arguments, a lesion $\hat{z}_t \in \hat{Z}_t$ from \mathcal{M}_t and $\hat{z}_{t+1} \in \hat{Z}_{t+1}$ from \mathcal{M}_{t+1} , are set to correspond, and 0 otherwise. We enforce $\sum_{\hat{z}_{t+1}} \pi(\hat{z}_t, \hat{z}_{t+1}) = 1$ so that a lesion in \mathcal{M}_t is mapped to a single lesion in \mathcal{M}_{t+1} .

We find an optimal π that minimizes a loss function \mathcal{L} , i.e.,

$$\pi^* = \underset{\pi}{\operatorname{argmin}} \mathcal{L}, \quad (7)$$

where \mathcal{L} is designed to encourage that (i) corresponding lesions \hat{z}_t in \mathcal{M}_t and \hat{z}_{t+1} in \mathcal{M}_{t+1} to be located at the same (or more proximate) anatomical locations, which is implemented as a unary term \mathcal{U} in \mathcal{L} ; and (ii) distances between any pair of lesions, $\hat{z}_t^{(i)}$ and $\hat{z}_t^{(j)}$, in \mathcal{M}_t to be identical (or more similar) to the distances between the corresponding pair of lesions, $\hat{z}_{t+1}^{(m)}$ and $\hat{z}_{t+1}^{(n)}$, in \mathcal{M}_{t+1} , which is implemented via a binary term \mathcal{B} in \mathcal{L} . Consequently, we write

$$\mathcal{L} = \alpha \mathcal{U} + (1 - \alpha) \mathcal{B}, \quad \alpha \in [0, 1] \quad (8)$$

$$\mathcal{U}(\pi, \hat{Z}_t, \hat{Z}_{t+1}) = \sum_{\hat{z}_t \in \hat{Z}_t, \hat{z}_{t+1} \in \hat{Z}_{t+1}} \pi(\hat{z}_t, \hat{z}_{t+1}) \cdot g(\hat{z}_t, \hat{z}_{t+1}) \quad (9)$$

$$\mathcal{B}(\pi, \hat{Z}_t, \hat{Z}_{t+1}) = \sum_{\substack{\hat{z}_t^{(i)}, \hat{z}_t^{(j)} \in \hat{Z}_t \\ \hat{z}_{t+1}^{(m)}, \hat{z}_{t+1}^{(n)} \in \hat{Z}_{t+1}}} \pi(\hat{z}_t^{(i)}, \hat{z}_{t+1}^{(m)}) \cdot \pi(\hat{z}_t^{(j)}, \hat{z}_{t+1}^{(n)}) \cdot |g(\hat{z}_t^{(i)}, \hat{z}_t^{(j)}) - g(\hat{z}_{t+1}^{(m)}, \hat{z}_{t+1}^{(n)})|, \quad (10)$$

where $|\cdot|$ is the absolute value and $g(\mu, \eta)$ returns a measure of distance between a pair of vertices μ, η (described below).

Optimization: When $\alpha = 1$, Eq. 8 contains only the unary term. This can be reformulated as a bipartite graph matching problem and optimized through the Kuhn–Munkres algorithm [Munkres, 1957]. When $0 < \alpha < 1$, a 2nd order regularization term is included in the matching loss, which we optimized using a tensor-based approach [Duchenne et al., 2011].

Selection of g : The selection of g could result in different optimization results. One selection of g is to set it as the Euclidean distance between two points in 3D. A second choice is to first determine anatomical correspondences between the two meshes, which anatomically registers the 3D coordinates of the lesions \hat{Z}_t and \hat{Z}_{t+1} , then calculate the geodesic distance for each pair of \hat{z}_t and \hat{z}_{t+1} on a 3D mesh. Specifically, with 3D registration \mathcal{D} , we have

$$g(\hat{z}_t, \hat{z}_{t+1}) = d_g(\mathcal{D}(\hat{z}_t), \hat{z}_{t+1}) \quad (11)$$

where d_g is the geodesic distance on \hat{Z}_{t+1} and $\mathcal{D}(\cdot)$ applies the 3D-CODED [Groueix et al., 2018] registration as described in Section II-C.

III. DATA ACQUISITION AND AUGMENTATION

To show the generalizability of the proposed approach over a variety of datasets, and to address the lack of 3D skin data with annotated skin lesions, we obtained 3D mesh and texture data from the following sources.

A. 3D Mesh Hand-held Acquisition

We scanned a mannequin using an Artec Eva 3D hand-held scanner [Artec, 2021] to generate 10 meshes. In each mesh, pen-drawn markers with varying shapes and sizes, body locations and numbers were attached to the mesh surface to represent synthetic skin lesions. We show an example scan in Fig. 5 and synthetic lesions in Fig. 6. The following describes the possible transforms applied to each synthetic lesion. The synthetic lesion can be applied to different *body locations*: {Chest, Abdomen, Arm Left, Arm Right, Thigh Left, Thigh Right, Back}. The synthetic lesion can have different *colours*: {black, brown, yellow, pink, orange, grey, red}. Finally, the synthetic lesion can have a circular *shape* with a diameters of {0.5, 1, 2} cm or an elliptical *shape* with minor/major axes of {(1, 2)} cm. Table II shows the applied transforms used to create the synthetic lesions.

B. Digital Static Model Preparation

Using 300 3D textureless (i.e., without skin colour) meshes from the FAUST dataset [Bogo et al., 2014a], we modified each mesh to create a total of 900 augmented meshes (Fig. 7). To augment each mesh we rig each model into three different postures using the quick rig tool [Autodesk Maya, 2020b]; assign a skin colour (RGB values) uniformly sampled from the Fitzpatrick scale to each individual mesh; add images of lesions sampled from the ISIC 2017 dataset [Codella et al.,

TABLE II: 10 scans (rows) with synthetic lesion properties applied to a specific mannequin pose, where a maximum of seven lesions were applied at once. Using the encoding described in Section III-A, the capital letters indicate the lesion *location*, the superscript indicates the lesion *colour*, and, the subscript indicates the lesion *shape*.

scan	Lesion Number						
	1	2	3	4	5	6	7
1	$A_{0.5}^{br}$	TL_1^r	TR_1^{bl}	$B_{(2,1)}^g$	B_2^p		
2	$AL_{0.5}^r$	AR_1^{bl}	TL_1^{br}	$B_{(2,1)}^g$	B_2^p	$B_{0.5}^o$	
3	AL_1^g	$AR_{0.5}^{br}$	TL_1^{br}	TR_1^{bl}	B_2^p	$B_{0.5}^r$	B_1^o
4	C_2^p	A_1^g	$AR_{0.5}^{br}$	TR_1^r			
5	C_1^g	A_2^p	AR_1^{br}	B_1^r	B_1^o		
6	AL_1^g	AR_2^p	TL_1^{br}	B_1^r	B_1^b		
7	A_1^g	AR_2^p	$TR_{0.5}^{br}$	B_1^r	B_1^b		
8	C_1^g	A_2^p	$TR_{0.5}^{br}$	B_1^o	$B_{0.5}^r$		
9	$AR_{0.5}^{br}$	$B_{(2,1)}^g$	B_2^p	$B_{0.5}^r$	B_1^{bl}		
10	$A_{(2,1)}^g$	AL_2^p	$TL_{0.5}^{br}$	B_1^{bl}	$B_{0.5}^r$	B_1^o	

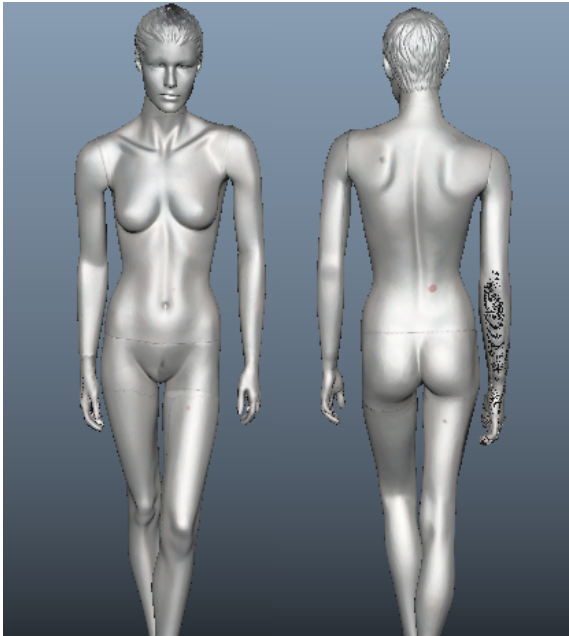


Fig. 5: Scanned mannequin with synthetic skin markers.

2018] to a 32×32 patch at a user-defined location on the mesh; and, apply UV unwrapping [Autodesk Maya, 2020a] to map the colours of the mesh to a 2D texture image I .

C. Annotating 3DBodyTex

To evaluate our approach on human subjects, with challenging visual artefacts (e.g., hair, cloths), we manually annotate

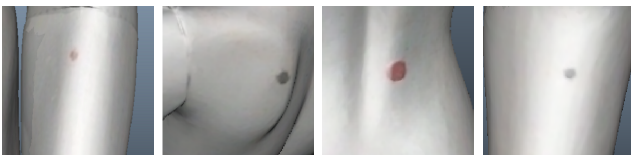


Fig. 6: Close-up examples of the synthetic skin markers applied to the mannequin.



Fig. 7: Augmented FAUST meshes with varying skin colour and postures.

candidate pigmented skin lesions visible on the 2D texture images provided by 3DBodyTex. We consider these manual annotations as “candidate” pigmented skin lesions since that although these regions appear to contain a pigmented skin lesion, given the scan resolution and the subjectivity of the human annotator, these may contain artefacts that are visually similar to lesions. These manual annotations are areas of interest that could be noted for the dermatologist to review.

To manually annotate the lesions within the texture images, we used the VGG Image Annotator (VIA) [Dutta and Zisserman, 2019, Dutta et al., 2016] to place bounding boxes around “candidate” lesions. To help standardize the annotations, the texture images were shown zoomed in between five and six times using VIA [Dutta et al., 2016]. As the precise boundary of the lesion is difficult to determine and our primary goal is to localize the lesions, we annotated with the goal of obtaining a lesion within the center of the bounding box, where some subjectivity to the size of the bounding box was allowed. To better account for differences among human annotations, three different human annotators annotated (Fig. 9) a subset of the meshes used to evaluate our R-CNN’s lesion detection performance (*static* test set used in Section IV-B1). To evaluate our lesion tracking approach, we used ten subjects scanned in two different poses and manually tracked ten lesions across the pairs of meshes (*longitudinal* test set used in Section IV-B2).

We manually annotated a total of 26,422 bounding boxes (including texture images annotated multiple times) from 218 3DBodyTex meshes, where the average width and height of the bounding boxes on the 2D texture images were 22.07 and 22.94 pixels respectively.

IV. EVALUATION AND DISCUSSION

To measure performance, object detection evaluations typically rely on a intersection over union (IoU) threshold score to determine a “correct detection” or a “match” between a detected and ground truth bounding box [Padilla et al., 2020]. However, in our pigmented skin lesion case, where the objects of interest occupy a fraction of the entire image, the manual annotations often contain a varying amount of the surrounding skin (Fig. 9). As our primary goal is to localize a bounding box that encapsulates the pigmented skin lesion rather than

obtaining the precise boundaries around the lesion, we define a metric based on overlapping centroids. Specifically, we define a “correct detection” or a “match” if both the centroids of the manually annotated box y and the model’s predicted box \hat{y} are enclosed by both,

$$(c(y) \in \hat{y}) \wedge (c(\hat{y}) \in y) \quad (12)$$

where $c(\cdot)$ computes the centroid of the box. Fig. 8 shows examples using the overlapping centroid metric on various bounding boxes.

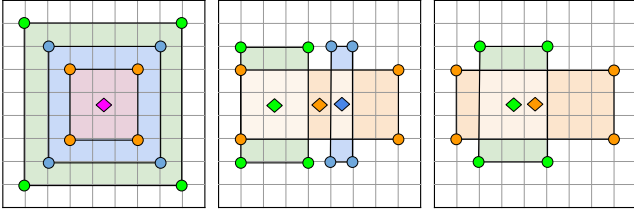


Fig. 8: (*left*) While the IoU differs among the green, blue, and orange boxes, they have the same centroid (diamond) and are considered as matching using the overlapping centroid metric. (*middle*) The orange box contains the centroid for the green and blue boxes; however, the green and blue boxes do not contain the centroid for the orange box, thus are not considered a match. (*right*) The green and orange boxes match as both contain each other’s centroids. Note that the green and orange boxes have the same IoU in the *middle* and *right* figures, but only the *right* figure shows a match using the centroid metric.

We report *recall*, which indicates the fraction of the manually annotated lesions the model detected; *precision*, which indicates the fraction of all the model’s predicted lesions that match with the manually annotated lesions; and, *average precision* (AP), which measures the area under the precision-recall curve for all the predicted confidence thresholds. To compute precision and recall, we use a confidence threshold of 0.5 to determine the predicted bounding boxes. We report results using both the IoU and overlapping centroid (Eq. 12) approaches, where an IoU threshold of greater than or equal to 0.5 determines a “correct detection” or a “match”.

A. Performance on FAUST and Mannequin Datasets

We trained a Faster R-CNN [Ren et al., 2016] to automatically predict the lesion bounding boxes on the FAUST dataset and the mannequin dataset. The Faster R-CNN has a backbone of a ResNet-50 network [He et al., 2016] pretrained on the COCO dataset [Lin et al., 2014]. For each spatial location, we generate 4 anchors of scale $\{32, 24, 16, 8\}$ with aspect ratio of $\{0.8, 1.0\}$. We optimized the network using stochastic gradient descent and a Bayesian hyperparameter search [Snoek et al., 2012] for 15 trials, with learning rate between $[1e-3, 1e-2]$, momentum between $[0.9, 0.99]$, and weight decay between $[1e-4, 1e-3]$ using a total of 20 epochs.

In our first experiment, we trained the R-CNN to detect lesions on the 900 augmented FAUST meshes (Section III-B). We performed three-fold cross validation and report the performance in Table III. For both the IoU and centroid (Eq. 12)

matching criteria, the precision, recall, and average precision of the proposed method is over 91%.

For our second experiment, we explore how well the model performance transfers onto a different dataset. We trained the R-CNN on the entire 900 samples from the augmented FAUST dataset (Section III-B) and used the trained model to detect the lesions from 10 random selected meshes of the scanned mannequin (Section III-A). Table IV shows the performance detecting the synthetic lesions on the scanned mannequin. While the performance does decrease when compared to the FAUST experiment, we highlight that our model is not trained on the mannequin data, and thus indicates the model has the capacity to generalize from digitally augmented models to a hand-held scanned model.

TABLE III: Three-fold cross validation performance when detecting the lesion present on each of the 900 augmented FAUST meshes. The results are computed over the entire fold and we report the average and standard deviation (in brackets) across the folds.

Match	Precision	Recall	AP
IoU	0.91 (0.01)	0.97 (0.01)	0.97 (0.00)
Centroid	0.91 (0.01)	0.98 (0.00)	0.98 (0.00)

TABLE IV: Performance over the mannequin with synthetic lesions applied. The results shown are averaged over each scan with the standard deviation among each scan shown in brackets.

Match	Precision	Recall	AP
IoU	0.83 (0.15)	0.58 (0.22)	0.63 (0.18)
Centroid	0.90 (0.14)	0.62 (0.20)	0.69 (0.14)

B. Performance on 3DBodyTex

In order to test our approach on more realistic data that exhibits additional real-world challenges (e.g., larger biological variation, hair, clothing), we rely on the 3DBodyTex [Saint et al., 2018] data composed of human textured meshes and the manual annotations as described in Section III-C. From the 200 subjects available in 3DBodyTex, we randomly partitioned the subjects into 120 training, 40 validation, 40 static testing subjects, where care was taken to ensure the subjects do not overlap across the partitions. 3DBodyTex has two scanned meshes of the same subject (total 400 meshes) and we select 10 longitudinal testing scans, which are a subset of the same subjects within the *static* testing partition, but in different body poses. We use the *longitudinal* testing partition to evaluate the lesion tracking component of our algorithm (Section II-D), where we manually tracked lesions in the *longitudinal* testing partition with the corresponding lesions in the *static* testing partition. Due to the effort required to manually track lesions across subjects, we only annotated and tracked a subset of the lesions (i.e., 10 corresponding lesions on each mesh) within the *longitudinal* testing partition. We note that both meshes were annotated for nine training subjects (218 out of 400 meshes were annotated, composed of 128 training meshes,

40 validation meshes, 40 static test meshes, 10 longitudinal test meshes) where we included the nine additional training mesh during training.

1) *Detecting Lesions on 3DBodyTex Textured Images*: We use the same Faster R-CNN as described in Section IV-A and fine-tune the network on the 3DBodyTex texture images using an initial learning rate of 0.001 for 20 epochs, followed by a learning rate of 0.0001 for 10 epochs. Due to GPU memory limitations, we divide the texture image (4096×4096 pixels) into 16 non-overlapping sub-images (1024×1024 pixels) and train using a batch size of 12 sub-images. We select the model weights that had the highest average precision score on the validation partition to evaluate the performance on the testing partition. We use non-maximum suppression with an IoU threshold of 0.01 to keep the highest scoring predicted bounding box when bounding boxes overlap.

Table V shows the performance over the static testing partition when considering bounding boxes from the three different human annotators (A1, A2, A3) as the source of “ground truth”. The reported metrics are improved using the centroid metric as overlapping bounding boxes that delineated different amounts of healthy skin were often considered incorrect using the IoU threshold matching criteria. We show an example of the variability of the human annotations in Fig. 9.

TABLE V: The performance on the static test partition when automatically detecting pigmented skin lesions within the 3DBodyTex dataset, where three different human annotators (A1, A2, A3) are considered as “ground truth”. The results shown are averaged over each scan with the standard deviation among each scan shown in brackets.

GT	Match	Precision	Recall	AP
A1	IoU	0.15 (0.12)	0.11 (0.08)	0.05 (0.06)
	Centroid	0.86 (0.08)	0.62 (0.13)	0.75 (0.11)
A2	IoU	0.60 (0.18)	0.73 (0.18)	0.66 (0.21)
	Centroid	0.71 (0.16)	0.85 (0.12)	0.85 (0.10)
A3	IoU	0.37 (0.15)	0.71 (0.26)	0.56 (0.24)
	Centroid	0.51 (0.16)	0.89 (0.16)	0.80 (0.12)

To further explore the performance of the machine annotations compared with human annotations, we set each annotator as the “ground truth” and compare the performance of the other annotators with respect to the “ground truth” annotator. Fig. 10 shows pair-wise precision, recall and F1-score, where each of the human and machine annotators act as the single source of ground truth and predictions. When considering the F1-score as a measure of agreement among annotators, we see that the two out of three human annotators agree more with the machine predictions than any other human annotator. This result suggests that the machine annotations perform favourably when considering the inter-rater variability among human annotations.

Additional qualitative results using our proposed method were shown in earlier figures. Fig. 2 shows the full texture image and the numerous lesions detected using the manual and automatically detected lesions. Fig. 3 shows the 3D mesh using the texture image marked with manually and automatically identified lesions.

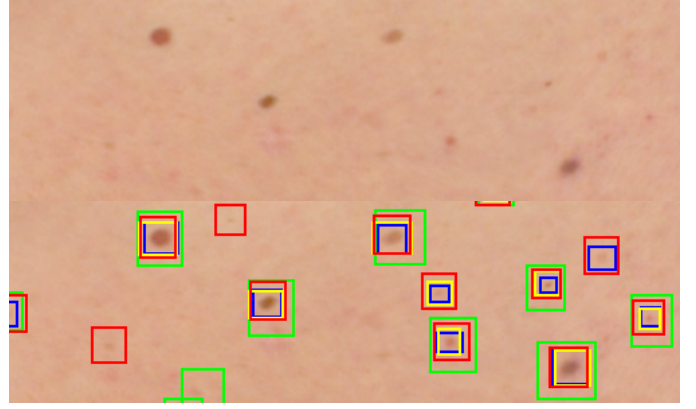


Fig. 9: The top image shows a zoomed in skin region without any annotations. The bottom image shows the same location but with three different human annotators (blue, green, and yellow boxes) and the machine bounding box predictions (red boxes). The differences among human annotators are shown (e.g., larger green boxes vs. the tight blue boxes) motivating our choice to use the centroid matching criteria that is not dependent on an IoU threshold.

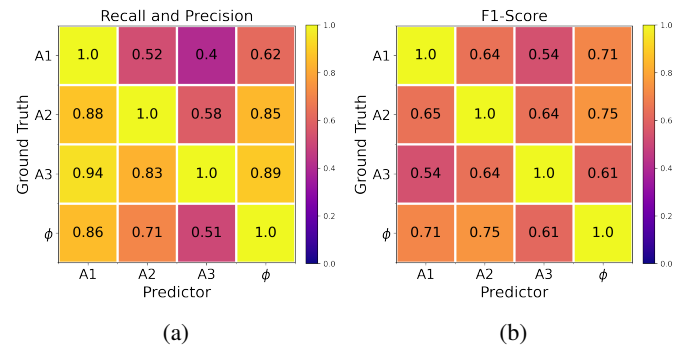


Fig. 10: Pair-wise performance on the static test set with three human annotators (A1, A2, A3) and the machine annotator (ϕ). The y-axis indicates which annotator was used as the ground truth, and the x-axis indicates which the annotator was used as the predictions. Each metric is computed per scan and averaged over all scans. (a) The upper and lower triangular matrix displays the recall and precision, respectively. (b). The F1-score combines recall and precision, and shows that the machine has a higher F1-score with two of the three human annotators than the human annotators have with any of each other.

2) *Tracking Lesions on 3DBodyTex*: We use the 3DBodyTex *longitudinal* testing partition (Section IV-B) to evaluate the tracking algorithm proposed in Section II-D. For each mesh belonging to the same subject, we gather the top- k scoring predicted bounding boxes that have scores greater than 0.5 using the trained R-CNN (Eq. 1), where k is the minimum number of detected lesions on a mesh of the same subject (we set a maximum value of $k = 100$). These detected bounding boxes serve as input to the tracking algorithm.

Table VI shows the *longitudinal* testing partition performance with 20 meshes representing 10 subjects, each with

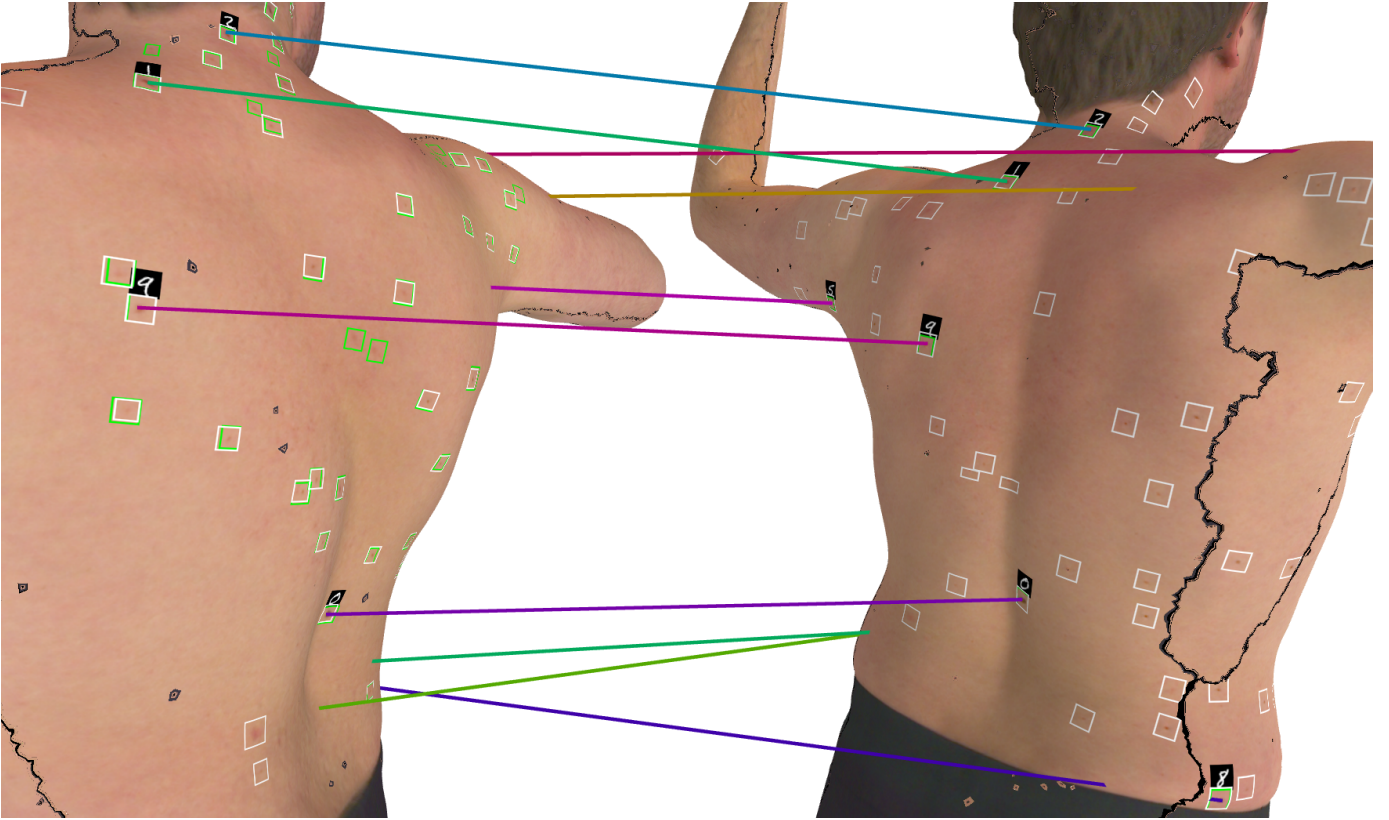


Fig. 11: Longitudinal tracking for a subset of the annotated lesions. The green boxes indicate the manual annotations. The white boxes indicate the automatic annotations. The coloured lines between the lesions indicate the automatically determined lesion correspondences for the subset of lesions we manually determined correspondences for (as represented by the numbers that indicate corresponding lesions determined manually). The dark curves on the meshes indicate the boundaries of the texture image seams. We note that the scan on the right is part of the longitudinal testing partition, and hence was not densely annotated.

10 pairs of corresponding lesions determined manually. These corresponding lesions represent a sample of the total lesions and, in general, are lesions that are more easily identifiable by the human eye. This is reflected in that our R-CNN achieves a high average recall (0.93), indicating that most of the longitudinal lesions were detected. To measure our performance on correctly tracking the same corresponding lesions across the meshes, we report a longitudinal accuracy metric that computes the fraction of the pairs of automatically detected longitudinal lesions correctly matched to the lesion in the corresponding mesh. We see that our full tracking method achieves an averaged accuracy of 80%, indicating that on average, 8 out of 10 lesions were correctly identified as being the same lesion across meshes. Fig. 11 shows qualitative results. We highlight that we only report results over the 10 pairs of manually matched lesions due to the manual effort required to determine correct lesion correspondences, but we perform our matching over a much larger set of detected lesion (on average, 60 detected lesions per scan).

V. CONCLUSIONS

We presented a novel pipeline for the detection and longitudinal tracking of skin lesions from 3D whole-body textured

TABLE VI: The performance using the pairs of lesions manually annotated within the longitudinal test partition. Each metric is computed per pair of meshes, and averaged across paired meshes with the standard deviation shown in brackets. *Recall* indicates the fraction of the longitudinal lesions that were automatically identified. In this case, precision is not a meaningful metric as not all the lesions are used for the longitudinal analysis. α indicates the weighting between the unary and binary term used in the tracking equation (Eq. 8), where $\alpha = 0.5$ uses only the unary term and $\alpha = 0.5$ equally weighs both terms. *Distance* indicates the type of distance measure used, where *Euclidean* considers the L_2 distances among vertex coordinates while *geodesic* uses the anatomical correspondence among vertices in paired scans to compute geodesic distances.

Recall	α	Distance	Accuracy
0.93 (0.10)	1	Euclidean	0.34 (0.21)
	0.5	Euclidean	0.26 (0.25)
	1	Geodesic	0.68 (0.23)
	0.5	Geodesic	0.80 (0.21)

surface scans. The whole-body field-of-view allows for encoding spatial relationships and capturing the global anatomical

context of lesions. The longitudinal analysis of body surface scans allows for monitoring and tracking changes in skin lesions across time, which may aid in early detection of melanoma.

Our novel approach of unwrapping the coloured 3D surface body scan into a 2D texture image can go beyond enabling the utilization of 2D Faster-RCNN to this 3D problem, to allowing leveraging general 2D computer vision techniques, e.g., other object detection methods, segmentation techniques, or image enhancement. However, we note that one of the limitations of detecting lesions on the 2D texture image is that, albeit rarely occurring, lesions that appear on the seams of the texture image may be challenging to identify. Future work may explore texture mappings that are split on non-lesion specific areas (e.g., cloths) or extending the 2D analysis to seam-aware methods.

While the skin lesions placed during the model augmentation process was done to simulate a more realistic task, future work would further expand on this to more realistic types of conditions outside of neoplasms. Future work would also apply our proposed approach onto scans of human subjects with a known range of diseases and incorporate a disease classification step. Further, future work should focus on studying skin colour bias, which may necessitate collecting datasets of more diverse populations with varying skin colours, as well as designing more advanced skin colour augmentation methods.

Given the rapid advancement in 3D scanning technologies in general, we anticipate that acquiring human body scans will become more convenient and popular (e.g., via smartphones), and more accurate. This, in turn, is expected to create more demand for developing improved methods for 3D skin surface analysis methods. We hope that the release of the mannequin data and the 3DBodyTex manual annotations will help facilitate research in this direction and be of use to the community.

ACKNOWLEDGMENTS

The funding for this work was provided by the Natural Sciences and Engineering Research Council of Canada (NSERC RGPIN-06752). The authors are grateful to Compute Canada and NVIDIA Corporation for providing the computational resources used in this research.

REFERENCES

- Naheed R. Abbasi, Helen M. Shaw, Darrell S. Rigel, Robert J. Friedman, William H. McCarthy, Iman Osman, Alfred W. Kopf, and David Polsky. Early diagnosis of cutaneous melanoma: revisiting the ABCD criteria. *The Journal of the American Medical Association*, 292(22):2771–2776, December 2004. doi: 10.1001/jama.292.22.2771. URL <https://doi.org/10.1001/jama.292.22.2771>.
- American Cancer Society. The American Cancer Society’s facts & figures: 2021 edition. <https://www.cancer.org/content/dam/cancer-org/research/cancer-facts-and-statistics/annual-cancer-facts-and-figures/2020/cancer-facts-and-figures-2020.pdf>, 2021. Accessed: March 31, 2021.
- Artec. Artec Eva. <https://www.artec3d.com/portable-3d-scanners/artec-eva-v2>, 2021. Accessed: March 29, 2021.
- Autodesk Maya. Maya Automatic UV mapping. <https://knowledge.autodesk.com/support/maya/learn-explore/caas/CloudHelp/cloudhelp/2020/ENU/Maya-Modeling/files/GUID-CD17C2C5-A442-4960-91DB-A2E5099EBF61-htm.html>, December 2020a. Accessed: November 12, 2020.
- Autodesk Maya. Maya Quick Rig tool. <https://knowledge.autodesk.com/support/maya/learn-explore/caas/CloudHelp/cloudhelp/2020/ENU/Maya-CharacterAnimation/files/GUID-DC29C982-D04F-4C20-9DBA-4BBB33E027EF-htm.html>, December 2020b. Accessed: November 12, 2020.
- Federica Bogo, Javier Romero, Matthew Loper, and Michael J. Black. FAUST: dataset and evaluation for 3D mesh registration. In *Computer Vision and Pattern Recognition*, pages 3794–3801, 2014a.
- Federica Bogo, Javier Romero, Enoch Peserico, and Michael J. Black. Automated detection of new or evolving melanocytic lesions using a 3D body model. In *International Conference on Medical Image Computing and Computer Assisted Intervention*, pages 593–600. 2014b.
- M. Emre Celebi, Noel Codella, and Allan Halpern. Dermoscopy image analysis: Overview and future directions. *IEEE Journal of Biomedical and Health Informatics*, 23(2): 474–478, 2019.
- Noel C. F. Codella, David Gutman, M. Emre Celebi, Brian Helba, Michael A. Marchetti, Stephen W. Dusza, Aadi Kalloo, Konstantinos Liopyris, Nabin Mishra, Harald Kittler, Allan Halpern, and Clifton Park. Skin lesion analysis toward melanoma detection: A challenge at the 2017 International Symposium on Biomedical Imaging (ISBI), hosted by the International Skin Imaging Collaboration (ISIC). In *IEEE International Symposium on Biomedical Imaging*, pages 168–172, 2018.
- Andrew Creadore, Sheena Desai, Sara J Li, Karen J Lee, Ai-Tram N Bui, Camila Villa-Ruiz, Kelly Lo, Guohai Zhou, Cara Joyce, Jack S Resneck, et al. Insurance acceptance, appointment wait time, and dermatologist access across practice types in the us. *JAMA dermatology*, 157(2):181–188, 2021.
- Theo Deprelle, Thibault Groueix, Matthew Fisher, Vladimir G. Kim, Bryan C. Russell, and Mathieu Aubry. Learning elementary structures for 3D shape generation and matching. In *Advances in Neural Information Processing Systems*, volume 32, pages 1–11, 2019.
- Olivier Duchenne, Francis Bach, In-So Kweon, and Jean Ponce. A tensor-based algorithm for high-order graph matching. *IEEE Transactions on Pattern Analysis and Machine Intelligence*, 33(12):2383–2395, 2011.
- A. Dutta, A. Gupta, and A. Zissermann. VGG image annotator (VIA). <http://www.robots.ox.ac.uk/~vgg/software/via/>, 2016. Version: 2.0.10, Accessed: March 22, 2021.
- Abhishek Dutta and Andrew Zisserman. The VIA annotation software for images, audio and video. In *Proceedings of the 27th ACM International Conference on Multimedia*, pages 2276–2279. ACM, 2019.

- Hao Feng, Juliana Berk-Krauss, Paula W Feng, and Jennifer A Stein. Comparison of dermatologist density between urban and rural counties in the united states. *JAMA dermatology*, 154(11):1265–1271, 2018.
- Sara Gandini, Francesco Sera, Maria Sofia Cattaruzza, Paolo Pasquini, Damiano Abeni, Peter Boyle, and Carmelo Francesco Melchi. Meta-analysis of risk factors for cutaneous melanoma: I. common and atypical naevi. *European Journal of Cancer*, 41(1):28–44, 2005.
- Thibault Groueix, Matthew Fisher, Vladimir G. Kim, Bryan C. Russell, and Mathieu Aubry. 3D-CODED: 3D Correspondences by deep deformation. In *ECCV*, volume LNCS 11206, pages 235–251, 2018.
- Holger A. Haenssle, Bianca Korpas, Christian Hansen-Hagge, Timo Buhl, Kjell M. Kaune, Steven Johnsen, Albert Rosenberger, Michael P. Schön, and Steffen Emmert. Selection of patients for long-term surveillance with digital dermoscopy by assessment of melanoma risk factors. *Archives of Dermatology*, 146(3), 2010.
- Kaiming He, Xiangyu Zhang, Shaoqing Ren, and Jian Sun. Deep residual learning for image recognition. In *IEEE Conference on Computer Vision and Pattern Recognition*, pages 770–778, 2016.
- Konstantin Korotkov, Josep Quintana, Susana Puig, Josep Malvehy, and Rafael Garcia. A new total body scanning system for automatic change detection in multiple pigmented skin lesions. *IEEE Transactions on Medical Imaging*, 34(1):317–338, 2015.
- Konstantin Korotkov, Josep Quintana, Ricard Campos, América Jesús-Silva, Pablo Iglesias, Susana Puig, Josep Malvehy, and Rafael Garcia. An improved skin lesion matching scheme in total body photography. *IEEE Journal of Biomedical and Health Informatics*, 23(2):586–598, 2019.
- Tim K Lee, M Stella Atkins, Michael A King, Savio Lau, and David I. McLean. Counting moles automatically from back images. *IEEE Transactions on Biomedical Engineering*, 52(11):1966–1969, 2005.
- Yunzhu Li, Andre Esteva, Brett Kuprel, Rob Novoa, Justin Ko, and Sebastian Thrun. Skin cancer detection and tracking using data synthesis and deep learning. In *AAAI Conference on Artificial Intelligence Joint Workshop on Health Intelligence*, 2017.
- Tsung-Yi Lin, Michael Maire, Serge Belongie, James Hays, Pietro Perona, Deva Ramanan, Piotr Dollár, and C Lawrence Zitnick. Microsoft COCO: Common objects in context. In *European Conference on Computer Vision*, pages 740–755, 2014.
- Bruce McGregor. Automatic registration of images of pigmented skin lesions. *Pattern Recognition*, 31(6):805–817, 1998.
- Hengameh Mirzaalian, Tim K. Lee, and Ghassan Hamarneh. Skin lesion tracking using structured graphical models. *Medical Image Analysis*, 27:84–92, 2016.
- James Munkres. Algorithms for the assignment and transportation problems. *Journal of the Society for Industrial and Applied Mathematics*, 5(1):32–38, 1957.
- Fulgencio Navarro, Marcos Escudero-Viñolo, and Jesús Bescós. Accurate segmentation and registration of skin lesion images to evaluate lesion change. *IEEE Journal of Biomedical and Health Informatics*, 23(2):501–508, 2019.
- Rafael Padilla, Sergio L. Netto, and Eduardo A. B. da Silva. A survey on performance metrics for object-detection algorithms. In *International Conference on Systems, Signals, and Image Processing*, pages 237–242, 2020.
- Riccardo Pampena, Athanassios Kyrgidis, Aimilios Lallas, Elvira Moscarella, Giuseppe Argenziano, and Caterina Longo. A meta-analysis of nevus-associated melanoma: Prevalence and practical implications. *Journal of the American Academy of Dermatology*, 77(5):938–945.e4, 2017.
- Sameena Pathan, K. Gopalakrishna Prabhu, and P. C. Siddalingaswamy. Techniques and algorithms for computer aided diagnosis of pigmented skin lesions - A review. *Biomedical Signal Processing and Control*, 39:237–262, 2018.
- Shaoqing Ren, Kaiming He, Ross Girshick, and Jian Sun. Faster R-CNN: Towards real-time object detection with region proposal networks. *IEEE Transactions on Pattern Analysis and Machine Intelligence*, 39(6):1137–1149, 2016.
- Alexandre Saint, Eman Ahmed, Abd El Rahman Shabayek, Kseniya Cherenkova, Gleb Gusev, Djamila Aouada, and Björn Ottersten. 3DBodyTex: Textured 3D body dataset. In *International Conference on 3D Vision*, pages 495–504, 2018.
- Gabriel Salerni, Cristina Carrera, Louise Lovatto, Joan Anton Puig-Butille, Celia Badenas, Estel Plana, Susana Puig, and Josep Malvehy. Benefits of total body photography and digital dermoscopy (“two-step method of digital follow-up”) in the early diagnosis of melanoma in patients at high risk for melanoma. *Journal of the American Academy of Dermatology*, 67(1):e17–e27, 2012.
- JK Schofield, D Fleming, D Grindlay, and H Williams. Skin conditions are the commonest new reason people present to general practitioners in england and wales. *British Journal of Dermatology*, 165(5):1044–1050, 2011.
- Richard Shellenberger, Mohammed Nabhan, and Sweta Kakaraparthi. Melanoma screening: A plan for improving early detection. *Annals of Medicine*, 48(3):142–148, 2016.
- Jasper Snoek, Hugo Larochelle, and Ryan P Adams. Practical Bayesian optimization of machine learning algorithms. In *Advances in Neural Information Processing Systems*, volume 25, pages 2951–2959, 2012.
- Luis R. Soenksen, Timothy Kassis, Susan T. Conover, Berta Marti-Fuster, Judith S. Birkenfeld, Jason Tucker-Schwartz, Asif Naseem, Robert R. Stavert, Caroline C. Kim, Maryanne M. Senna, José Avilés-Izquierdo, James J. Collins, Regina Barzilay, and Martha L. Gray. Using deep learning for dermatologist-level detection of suspicious pigmented skin lesions from wide-field images. *Science Translational Medicine*, 13(581):eabb3652, 2021.
- Wiebke Sondermann, Jochen Sven Utikal, Alexander H Enk, Dirk Schadendorf, Joachim Klode, Axel Hauschild, Michael Weichenthal, Lars E French, Carola Berking, Bastian Schilling, Sebastian Haferkamp, Stefan Fröhling, Christof von Kalle, and Titus J. Brinker. Prediction of melanoma evolution in melanocytic nevi via artificial intelligence: A call for prospective data. *European Journal of Cancer*, 119:

30–34, 2019.

Jennifer L. Strunck, Tristan C. Smart, Kenneth M. Boucher, Aaron M. Secrest, and Douglas Grossman. Improved melanoma outcomes and survival in patients monitored by total body photography: A natural experiment. *Journal of Dermatology*, 47(4):342–347, 2020.

Philipp Tschandl. Sequential digital dermatoscopic imaging of patients with multiple atypical nevi. *Dermatology Practical & Conceptual*, 8(3):231–237, 2018.